



# Sensitivity of visible range multi-wavelength algorithms for retinal tissue oximetry to acquisition parameters

CLÉOPHACE AKITEGETSE,<sup>1,\*</sup>  JASMINE POIRIER,<sup>1</sup> AND DOMINIC SAUVAGEAU<sup>1,2</sup>

<sup>1</sup>*Zilia inc., Québec, QC, G1K 3G5, Canada*

<sup>2</sup>*Chemical and Materials Engineering, University of Alberta, Edmonton, AB, T6G 1H9, Canada*

\*[cleo@ziliahealth.com](mailto:cleo@ziliahealth.com)

**Abstract:** This study examined the sensitivity of broadband spectroscopy algorithms for retinal tissue oximetry to spectral acquisition parameters. Monte Carlo simulations were conducted on a 4-layer retinal model to assess the impact of various parameters. The optimal spectral range for accurate measurements was determined to be 530 nm to 585 nm. Decreased spectral resolution below 4 nm significantly reduced accuracy. Using an acquisition area larger than the blood vessel resulted in an underestimation of oxygen saturation, especially for high values. A threshold was observed where increased light intensity had no significant impact on measurement variability. The study highlights the importance of informed parameter selection for accurately assessing retinal microcapillary oxygenation and studying local hemodynamics.

© 2023 Optica Publishing Group under the terms of the [Optica Open Access Publishing Agreement](#)

## 1. Introduction

Oxygenation plays a crucial role in maintaining physiological and functional activity of organs and tissues. Local abnormalities in oxygenation and oxygen regulation occur at the onset or with the development of many pathologies. For example, a decrease in oxygenation has been shown to be a distinguishing factor for tumors malignity [1,2], while some people with diabetes mellitus have their lower limbs poorly supplied with oxygen, thus causing diabetic foot [3]. A link has also been established between poor tissue oxygenation and other diseases such as ischemia reperfusion injury [4]. This is also true in the tissues of the eye: studies have shown that oxygen dysregulation is associated with several ocular pathologies including glaucoma [5–10], diabetic retinopathy [5,6,11–14], retinal vessel occlusions [5,6,15,16], retinitis pigmentosa [17,18], and age-related macular degeneration [19].

Blood oxygen saturation is one of the key parameters in the assessment of tissue oxygenation. Oximetry, the measure of this parameter, through optical and non-invasive methods exploits the reversible binding of oxygen to hemoglobin and the accompanying changes to the absorption spectrum, discovered by Stokes in the late 1800s [20]. Typically, a light source is used to illuminate the tissue to be probed, and two- or more wavelengths from the reflectance signal acquired by a light detector are used to determine oxygen saturation [3,21–34]. While two-wavelength techniques have been used successfully to measure arterial oxygen saturation [21] and in large blood vessels of the eye fundus [25], multiple wavelengths are generally required for measurement in tissue, mainly due to the scattering of tissue structures, the presence of other absorbers (such as melanin), and sensitivity to noise [26,27,35].

Regardless of the oximetry technique, a careful choice of wavelengths for analysis and spectral resolution is essential. The spectral resolution is determined by the bandwidth of the filters or by the spectrometer used, depending on the technology. However, the effect of spectral resolution on the accuracy of blood oxygen saturation calculations remains unclear. Also, even if it is

commonly accepted that noise can affect the validity and accuracy of calculated oximetry values [36], very few studies quantifying this effect are available to date.

We recently proposed an ocular oximetry method for calculating blood oxygen saturation in the tissues of the eye fundus from a diffuse reflectance spectrum in the visible light region, along with the method for assessing its accuracy [37]. In the present study, we used Monte Carlo simulations to investigate the impact of different spectral acquisition parameters on the accuracy of the said ocular oximetry technique. We show the effect of wavelength range, spectral resolution, light intensity, noise and background tissue reflectance. A comparison of the performance of the present method with that of two- and three-wavelength oximetry methods in the face of the variation of these parameters was also carried out.

## 2. Material and methods

### 2.1. Monte-Carlo simulations

Monte Carlo simulations of light transport in the eye fundus tissues, built on a previously demonstrated simulation architecture [37], were used to study the effect of different acquisition parameters. A modified version of *mcxyz* [38], a program allowing the simulation of the propagation of photons in a multilayered tissue, was used for the simulations. Each layer was defined based on absorption ( $\mu_a$ ) and scattering ( $\mu_s$ ) coefficients, anisotropy of scattering, refractive index and thickness. After its initial launch with unit weight, each photon propagated one step based on a random sampling of the probability density function  $1/(\mu_s + \mu_a)$ , followed by a weight attenuation,  $\mu_a/(\mu_s + \mu_a)$ , due to absorption by the tissue. After absorption, the attenuated photon was scattered along the deflection and azimuthal scattering angles, where the Henyey-Greenstein phase function was used to establish the deflection scattering angle. A refraction event was created when the propagation step occurred at the interface between 2 layers. The photon continued to propagate until its weight fell below a certain threshold, where a procedure called roulette was used to decide whether the photon was completely extinguished or not. The modification we introduced to the original model defined an acquisition region, called the region of spectral acquisition (ROSA). Only back-scattered photons having passed through the ROSA before exiting the tissue by the back surface were counted. All other exiting photons were ignored in the count. This allowed the placement of the probed region anywhere in the model.

As shown in Fig. 1, a simplified four-layer model - composed of the neural retina, the retinal pigment epithelium (RPE), the choroid and the sclera - was developed. Blood vessels ranging in radius from 6.25  $\mu\text{m}$  to 50  $\mu\text{m}$  were located within the neural retina. The same scattering coefficients and anisotropy that had been used in [37] were kept for all the layers. Absorption was determined by the blood content in the neural retina; thus, no absorption was considered outside the blood vessels. The absorption in the RPE was modeled by the concentration of melanin, which was set at 400 mmol/l. Absorption of the choroid is a function of hemoglobin and melanin contents. The hemoglobin concentration in the choroid was set to 1.7 mmol/l [39,40] and the melanin was set to 100 mmol/l. The choroidal blood oxygen saturation was set at 95%. As for the sclera, the absorption properties measured and published by Hammer *et al.* [39,41] were used. Table 1 shows an overview of the parameters used in the model, at 4 wavelengths.

Photons at each wavelength from 500 nm to 650 nm in 2-nm steps were propagated through the eye fundus model while tracing all the layers that had been crossed, and back-scattered photons were collected on the surface. In the model, we defined a spherical ROSA within one of the vessels. Only a back-scattered photon having at one time or another passed through the ROSA was accounted for in the reconstruction of the reflectance spectrum. By default, unless otherwise specified, a 50  $\mu\text{m}$  radius ROSA was positioned in a 50  $\mu\text{m}$  radius blood vessel and reflectance spectra were reconstructed from simulations of 20 actual oxygen saturation ( $\text{StO}_2$ ) values ranging from 1% to 100%; each spectrum being reconstructed with 2-nm wavelength steps.

**Table 1. Overview of the optical parameters in the Monte-Carlo model of the eye fundus. RPE and choroidal melanin concentrations were set to 400 mmol/l and 100 mmol/l, respectively. The choroidal StO<sub>2</sub> was 95%.**

		530 nm	550 nm	570 nm	590 nm
Blood	$\mu_a(\text{cm}^{-1})$	199.99	265.26	248.14	115.43
	$\mu_s(\text{cm}^{-1})$	94.34	90.91	87.72	84.75
	$g(-)$	0.90	0.90	0.90	0.90
Retina	$\mu_a(\text{cm}^{-1})$	6.00	7.96	7.44	3.46
	$\mu_s(\text{cm}^{-1})$	83.71	79.53	75.04	70.42
	$g(-)$	0.97	0.97	0.97	0.97
RPE	$\mu_a(\text{cm}^{-1})$	1097.69	948.76	825.76	737.03
	$\mu_s(\text{cm}^{-1})$	684.77	676.81	680.74	688.74
	$g(-)$	0.84	0.84	0.84	0.84
Choroid	$\mu_a(\text{cm}^{-1})$	435.24	423.90	389.12	251.44
	$\mu_s(\text{cm}^{-1})$	942.20	950.44	935.17	898.71
	$g(-)$	0.87	0.87	0.87	0.87
Sclera	$\mu_a(\text{cm}^{-1})$	4.79	4.39	4.03	3.74
	$\mu_s(\text{cm}^{-1})$	1004.67	949.39	883.92	862.88
	$g(-)$	0.90	0.90	0.90	0.90

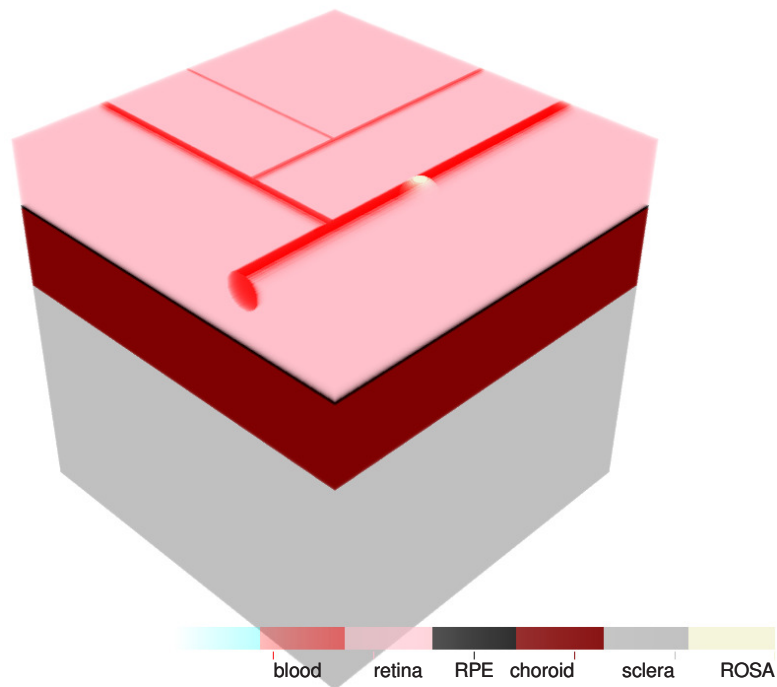


**Fig. 1.** Geometry of the Monte Carlo eye model. The neural retina, the RPE, the choroid and the sclera had thicknesses of 200  $\mu\text{m}$ , 10  $\mu\text{m}$ , 250  $\mu\text{m}$  and 700  $\mu\text{m}$ , respectively. The largest blood vessel was 50  $\mu\text{m}$  in radius and the smallest was 6.25  $\mu\text{m}$  in radius. The ROSA is indicated at a beige area

## 2.2. Eye fundus reflectance model

The eye fundus reflectance model was based on the modified Beer-Lambert law. This law is widely used in eye fundus oximetry applications [29,37,42,43], the diffusion theory being ill-suited for this case because absorption is more significant than scattering [44].

The eye fundus optical density is estimated by

$$OD(\lambda) = c_0 + c_S \log \frac{1}{\lambda} + c_{HbO} \varepsilon_{HbO}(\lambda) + c_{HbR} \varepsilon_{HbR}(\lambda) + c_M \varepsilon_M(\lambda) + c_L S_L(\lambda), \quad (1)$$

where  $OD(\lambda)$ ,  $\varepsilon_{HbO}$ ,  $\varepsilon_{HbR}$ ,  $\varepsilon_{MeI}$  and  $S_{lens}$  are the eye fundus optical density (OD), the oxy-hemoglobin molar extinction coefficient, the deoxy-hemoglobin molar extinction coefficient, the melanin molar extinction coefficient and the crystalline lens reference OD respectively. The term  $c_S \log \frac{1}{\lambda}$  is an empirical model of scattering, including erythrocyte light scattering [29], and  $c_0$  is a scaling term.

In Eq. (1),  $c_{HbO}$  and  $c_{HbR}$  are coefficients representing products of the average optical path length of the light through blood and the concentration of oxy- and deoxy-hemoglobin, respectively. The spectrum which would be acquired by a spectrometer collecting the light reflected from the eye fundus is expressed by Eq. (2),

$$I(\lambda) = I_0(\lambda) \exp(-OD(\lambda)), \quad (2)$$

where  $I(\lambda)$  is the noise-free diffuse reflectance spectrum and  $I_0(\lambda)$  the spectrum of the incident light.

In real conditions, the acquired spectrum contains spurious signals, such as the ambient light spectrum, specular reflections and other noises. The ambient light spectrum can generally be well characterized and subtracted from the acquired signal. The acquired spectrum is particularly affected by shot noise, inherent in the particulate nature of light, whose distribution follows Poisson's law [45,46]. The combination of remaining noises can be considered to have a Gaussian distribution with a zero mean [45,46]. Therefore, the spectrum affected by noise can be represented by Eq. (3),

$$I_N(\lambda) = \text{Poisson}(I(\lambda)) + \text{Gaussian}(0, \sigma), \quad (3)$$

where  $I_N(\lambda)$  is the noise-affected spectrum,  $I(\lambda)$  is the noise-free spectrum as expressed in Eq. (2) and  $\sigma$  is the standard deviation of the Gaussian noise.

### 2.2.1. Multi-wavelength method for oximetry

Calculating  $StO_2$  from a continuous spectrum is done by solving Eq. (1) in order to find the parameters  $c_{HbO}$  and  $c_{HbR}$ , and finally calculating  $StO_2$ , which is the ratio between the amount of oxygenated hemoglobin and the total amount of hemoglobin (Eq. (4)).

$$StO_2 = \frac{c_{HbO}}{c_{HbO} + c_{HbR}} \times 100. \quad (4)$$

A two-step method for solving Eq. (1) has already been described elsewhere [37]. It consisted, in a first step, in solving the Eq. (1) by a least-squares fitting method over a wide spectral range (500 nm to 650 nm). This first step allowed an estimation of the coefficients of scattering, melanin and crystalline lens terms,  $\hat{c}_S$ ,  $\hat{c}_M$  and  $\hat{c}_L$ , respectively. These coefficients were then used to get an estimate of a new optical density, largely dominated by the absorption of hemoglobin,

$$\begin{aligned} OD_{Hb}(\lambda) &= OD(\lambda) - \hat{c}_S \log \frac{1}{\lambda} - \hat{c}_M \varepsilon_M(\lambda) - \hat{c}_L S_L(\lambda), \\ &\approx c_0 + c_{HbO} \varepsilon_{HbO}(\lambda) + c_{HbR} \varepsilon_{HbR}(\lambda), \end{aligned} \quad (5)$$

which is solved using a least-squares fitting method on a narrower spectral range getting  $c_{HbO}$  and  $c_{HbR}$ , used in Eq. (4).

In this study, we refer to this method as the **multi-wavelength method**.

### 2.2.2. Two-wavelength method for oximetry

The two-wavelength method is derived directly from Eq. (5) [47]. By replacing  $c_{\text{HbO}}$  and  $c_{\text{HbR}}$  by a function of  $\text{StO}_2$  and, considering the cases where the scale term  $c_0$  is zero,  $\text{OD}_{\text{Hb}}(\lambda)$  can be written as

$$\text{OD}_{\text{Hb}}(\lambda) = \text{BT} (\text{StO}_2 (\varepsilon_{\text{HbO}}(\lambda) - \varepsilon_{\text{HbR}}(\lambda)) + \varepsilon_{\text{HbR}}(\lambda)), \quad (6)$$

where  $\text{BT} = c_{\text{HbO}} + c_{\text{HbR}}$ . Since all variables of Eq. (6) are known except for  $\text{BT}$  and  $\text{StO}_2$ , values of  $\text{OD}_{\text{Hb}}$  at the wavelengths  $\lambda_1$  and  $\lambda_2$  suffice to solve the equation. One of the wavelengths ( $\lambda_1$  in the present case) can be chosen from an isosbestic point, i.e.  $\varepsilon_{\text{HbR}}(\lambda_1) = \varepsilon_{\text{HbO}}(\lambda_1)$ , to simplify the calculations. From this, one obtains

$$\text{StO}_2 = m \times \frac{\text{OD}_{\text{Hb}}(\lambda_2)}{\text{OD}_{\text{Hb}}(\lambda_1)} + b, \quad (7)$$

where  $m$  and  $b$  are functions of  $\varepsilon_{\text{HbO}}(\lambda_2)$ ,  $\varepsilon_{\text{HbR}}(\lambda_2)$  and  $\varepsilon_{\text{HbR}}(\lambda_1)$ .

In practice, the coefficients  $m$  and  $b$  are obtained by calibration from reference structures or samples where  $\text{StO}_2$  values are known [25,48]. In this study, we calibrated the method by using the OD obtained by simulations of two blood vessels where the  $\text{StO}_2$  were 0% and 100%, using the two wavelengths 560 nm and 586 nm.

### 2.2.3. Three-wavelength method for oximetry

Three-wavelength methods add a term accounting for scattering to Eq. (6).

$$\text{OD}_{\text{Hb}}(\lambda) = \text{BT} (\text{StO}_2 (\varepsilon_{\text{HbO}}(\lambda) - \varepsilon_{\text{HbR}}(\lambda)) + \varepsilon_{\text{HbR}}(\lambda)) + B(\lambda), \quad (8)$$

By using two isosbestic wavelengths  $\lambda_1$  and  $\lambda_2$ , to eliminate  $\text{StO}_2$  from the equation, and choosing them close enough together ( $B(\lambda_1) \approx B(\lambda_2)$ ), it becomes possible to solve the equation and obtain the parameter  $B(\lambda)$  [26,27]. The last step is to use a third non-isosbestic wavelength  $\lambda_3$  to calculate  $\text{StO}_2$  from Eq. (8). In this study, we used the isosbestic wavelengths 569 nm and 586 nm, and the non-isosbestic wavelength 558 nm, as has been done in a study by Delori [27].

## 3. Results

### 3.1. Spectral range for multi-wavelength oximetry

Whether using two, three, four or multiple wavelengths, calculations to determine oxygen saturation in the eye fundus from reflected light are typically made in the spectral region between 500 nm and 600 nm [27,35,42,48–50]. Within this region, however, the selection of spectral range varies from method to method.

In order to investigate the effect of the selected spectral range on the  $\text{StO}_2$  accuracy, five million photons per wavelength were propagated in the eye fundus model. The multi-wavelength method was used to determine the  $\text{StO}_2$  with the narrow spectral band (the one used in the second step of the method) set to 18 different spectral ranges. When dealing with the eye fundus reflectance, it has been shown that for wavelengths greater than 590 nm, the contribution of the choroidal blood vessels increases and interferes with the signal from the retinal blood vessels [42]. On the other hand, light scattering increases for shorter wavelengths, leading to deviations in the oximetry empirical model [29]. Based on this, the spectral ranges tested were contained with 510–590 nm. Figure 2 shows the scatter plots of calculated and actual  $\text{StO}_2$  values obtained for the ranges of 510–590 nm and 530–585 nm. Although the slopes of the two trends are different, strong linear correlations exist for both ranges between the calculated and the actual values. This was also the case for all ranges tested. The Pearson's correlation coefficient was greater than 0.999 (except

for the ranges 540-585 nm and 540-580 nm, where it was 0.996 and 0.991, respectively) and the p-value, for a statistical test where the null hypothesis is a slope equal to zero, was zero. The slope and the intercept are presented in Figure 3. From this figure, we see that the range of 530-585 nm gave the best agreement between the calculated  $\text{StO}_2$  and the actual values.

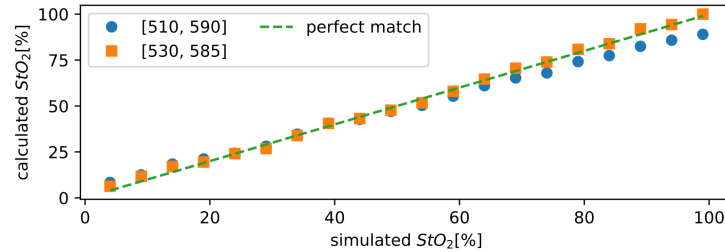


**Fig. 2.** Selection of the spectral range. Scatter plots of  $\text{StO}_2$  values calculated by the multi-wavelength method versus expected values, when the narrow spectral band is set to 510-590 nm and 530-585 nm. Perfect match is indicated as a dashed line. The data from the 16 other spectral ranges tested displayed similar trends and is shown in Supplemental Figures S1 to S5.

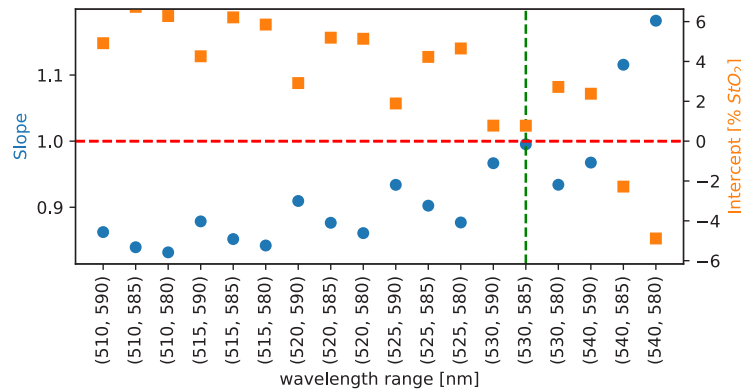


**Fig. 3.** Coefficients of regressions between calculated and actual  $\text{StO}_2$  for varying wavelength ranges. The dashed horizontal line indicates the level where a perfect match is reached - the slope is 1 and the bias is 0 - while the dashed vertical line highlights the spectral range closest to that perfect match.

### 3.2. Impact of spectral resolution on multi-wavelength oximetry

Investigation of the effect of the spectral resolution on the accuracy of the multi-wavelength method was carried out using spectra generated by the propagation of five million photons in the eye fundus model. In order to simulate a change in spectral resolution, the spectra were convolved with a Gaussian function whose width would determine the spectral resolution  $\Delta\lambda = 2 \text{ nm} \times 2.355\sigma$ , where  $\Delta\lambda$  is the spectral resolution and  $\sigma$  is the standard deviation of the Gaussian function. The spectra were subsequently used to calculate the  $\text{StO}_2$ .

Figure 4 shows the correlations between the  $\text{StO}_2$  obtained with five different resolutions, varying from 1.2 nm to 10.6 nm, and the actual values. In each case, a linear correlation exists between these parameters; however, we observe an underestimation of the values when the resolution decreases. This underestimation is more important with greater values of the actual



StO<sub>2</sub>, as evidenced by the increasing deviation from the perfect match case with increasing values.

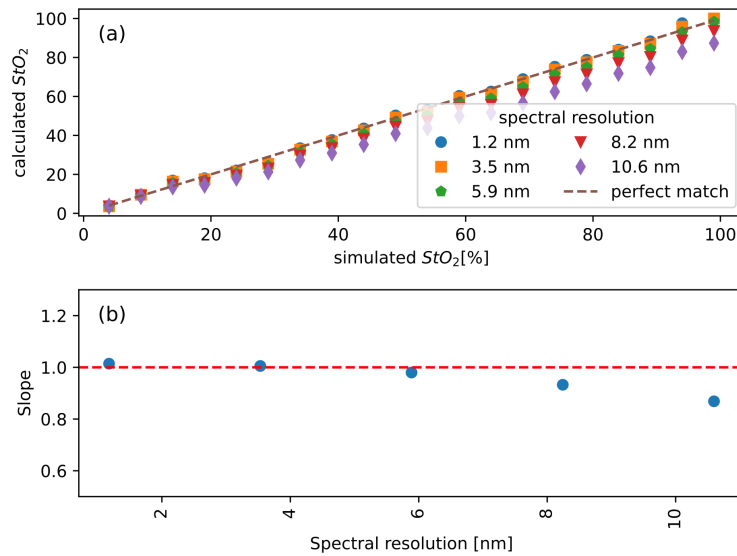


**Fig. 4.** Impact of spectral resolution on the estimation of StO<sub>2</sub> using multi-wavelength methods. (a) Scatter plot of calculated StO<sub>2</sub> values using different spectral resolutions, versus the simulated values. Perfect match is indicated as a dashed line. (b) Slope of the correlation between calculated and actual StO<sub>2</sub> for different spectral resolutions.

### 3.3. Impact of noise on diffuse reflectance spectra

Several sources of noise can affect spectra, which could have an impact on the accuracy of StO<sub>2</sub> calculations. Shot noise results from the statistical variation in the rate of photon reaching the detector, which in turn depends on the amount of light used to illuminate the sample. In the literature, the number of photons used in Monte Carlo simulations for studies involving the eye fundus varies greatly – e.g. ranging from 100,000 to five million [37,40,51,52] –, often as a compromise to reduce simulation time.

To evaluate the effect of the number of photons used in simulations would have on the calculated StO<sub>2</sub> accuracy, we ran successive simulations with 100,000, 500,000, 1 million, 2 million and 5 million photons. The multi-wavelength method was used to calculate the StO<sub>2</sub>.

Table 2 shows that the number of photons used in the simulation had no noticeable effect on the linear correlation between the calculated and the actual values. However, as expected, the quality of the correlations increased with increasing number of photons, as can be seen with the increasing Pearson correlation coefficient.

For comparison purposes, we also calculated the StO<sub>2</sub> for varying amounts of photons using the two- and three-wavelength methods, and the root-mean-square error (RMSE) was calculated in each case. Results are shown in figure 5, which shows a decrease in the calculated StO<sub>2</sub> RMSE for the three methods tested as the number of photons increased from 100,000 to five million. The RMSE trends were similar for the two- and three-wavelength methods, which both showed greater RMSE (approximately 4 times greater regardless of the number of photons used) than the multi-wavelength method.

The collected signal can also be affected by other types of noise characterized by a Gaussian distribution, largely dominated by readout noise. These are random, wavelength-independent noises that add to the actual reflected spectrum. To study the effect of Gaussian additive noise on

**Table 2. Linear regression coefficients and Pearson correlation coefficients of relationship between calculated and actual StO<sub>2</sub>, with varying number of photons in Monte Carlo simulations.**

Number of photons	Slope	Intercept	Pearson's R
$1 \times 10^5$	1.105	-1.634	0.942
$5 \times 10^5$	1.006	-0.261	0.984
$1 \times 10^6$	1.023	-2.135	0.995
$2 \times 10^6$	1.003	-1.642	0.995
$5 \times 10^6$	1.010	-0.278	0.998

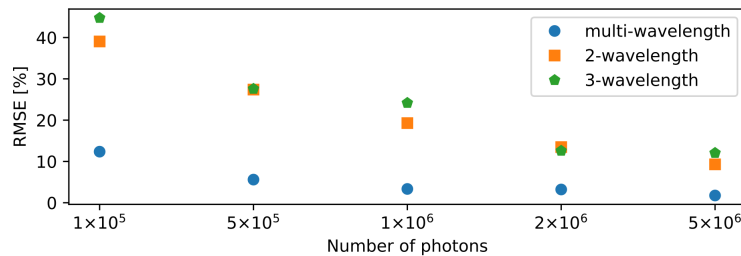


**Fig. 5.** Impact of light intensity on the calculated StO<sub>2</sub>. Root-mean-square error (RMSE) as a function of the number of photons used in Monte Carlo simulations. The two- and three-wavelength methods RMSE was approximately 4-fold that of the multiwavelength method, regardless of the number of photons used.

the estimation of StO<sub>2</sub>, we propagated photons in the Monte Carlo model of the eye fundus with a ROSA positioned inside a blood vessel. Four noise levels were added to each of the spectra using Eq. (3). Shot noise was kept low by using 5 million photons for each simulation. The multi-wavelength method was used to calculate the StO<sub>2</sub>.

Table 3 shows that the Gaussian-distributed additive noise does not alter the linear correlation between the estimated and the actual StO<sub>2</sub> values. In this case, the Pearson correlation coefficients decreased with increasing NSR, which is consistent with a decreasing accuracy with increasing noise.

**Table 3. Linear regression and Pearson correlation coefficient of relationships between calculated and actual StO<sub>2</sub> with varying noise-to-signal ratio (NSR).**

NSR	Slope	Intercept	Pearson's R
0.000	1.010	-0.278	0.998
0.025	0.998	-1.971	0.992
0.050	0.984	-0.725	0.965
0.075	0.923	+2.259	0.918
0.010	1.102	-1.340	0.940

The RMSE of the resulting simulations for the three calculation methods is shown in Figure 6. As can be seen, RMSE increases as the noise-to-signal ratio (NSR) is increased. But again, in this case, the RMSE for the two- and three-wavelength methods are approximately 4-fold greater than that of the multi-wavelength method.



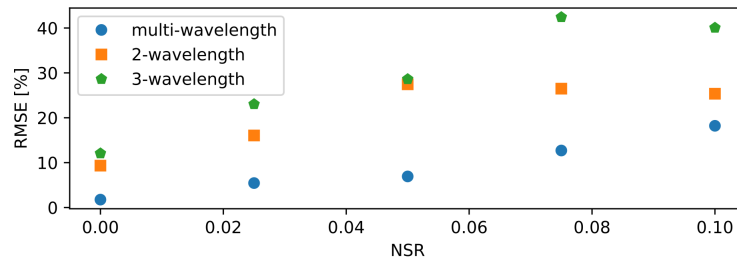


**Fig. 6.** Impact of additive Gaussian noise on the calculation of  $\text{StO}_2$ . RMSE between the calculated and the actual  $\text{StO}_2$  values as a function of NSR.

### 3.4. Relative importance of wavelengths in multi-wavelength oximetry

When developing a multi-wavelength methods, it is important to determine the potential impact of a disturbance of the reflectance spectrum on a single wavelength. The reflectance spectrum was disturbed at the selected wavelength by increasing the initial value by an amplitude varying from 1% to 20%. The  $\text{StO}_2$  was calculated using the multi-wavelength method, and the RMSE between the calculated and the actual values was determined. Wavelengths between 530 nm and 585 nm were disturbed with a 2-nm step. As can be seen in figure 7, the RMSE increased with the amplitude of the disturbances for a large majority of the wavelengths. However, it should be noted that the magnitude of the increase in RMSE differed from one wavelength to another, being very low at 570 nm and reaching a local maximum at 560 nm and tending towards greater values at both ends of the range tested (530 nm and 584 nm).

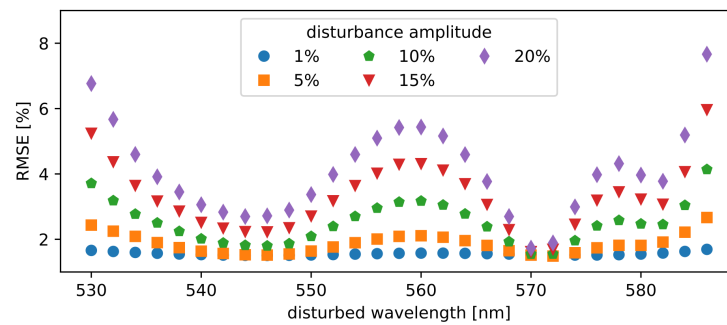


**Fig. 7.** Relative importance of individual wavelengths using the multi-wavelength method. RMSE between the calculated and the actual  $\text{StO}_2$  values as disturbances (1%, 5%, 10%, 15% and 20%) were introduced in the reflectance intensity at specific wavelengths. The multi-wavelength method was used for  $\text{StO}_2$  calculations.

In order to compare the performance of the multi-wavelength method with those of the two- and three-wavelength methods,  $\text{StO}_2$  was calculated from the disturbed spectra with each, only considering the relevant wavelengths in the latter two. Table 4 shows the RMSE obtained for the two-wavelength and three-wavelength method, respectively.

The results reveal that both methods are very sensitive to noise, with a 1% disturbance on a single wavelength having a greater impact on them (over 8% increase in RMSE for both cases) than a 20% disturbance on any of the wavelengths used in the multi-wavelength method (maximum RMSE of 7.65% at 584 nm).

**Table 4. RMSE between actual  $\text{StO}_2$  and  $\text{StO}_2$  calculated with the 2-wavelength and 3-wavelength methods when disturbances are applied to a single wavelength.**

Disturbance amplitude	2-wavelength		3-wavelength		
	560 nm	586 nm	558 nm	569 nm	586 nm
1%	8.5	8.6	8.5	5.7	5.8
5%	19.3	20.1	19.2	11.3	6.4
10%	35.4	36.5	31.1	19.4	10.3
15%	51.3	52.2	40.9	25.7	15.2
20%	66.6	67.0	47.8	30.6	18.7

### 3.5. Overlap of the ROSA on the background tissue

The ROSA size is dictated by technological choices, and it can be challenging to achieve a small size ROSA that fits entirely within a blood vessel [53].

We therefore wanted to study the effect, on the calculated  $\text{StO}_2$ , of the overlap of the ROSA with the tissue surrounding a blood vessel. To do this, we performed Monte Carlo simulations with ROSAs of varying radii - 50  $\mu\text{m}$ , 75  $\mu\text{m}$ , 100  $\mu\text{m}$  and 125  $\mu\text{m}$  - while maintaining a blood vessel of 50  $\mu\text{m}$  in radius. All three  $\text{StO}_2$  calculation methods were evaluated. It can be seen from the results, shown in figure 8, that the RMSE increased with the ROSA radius for all methods. However, the multi-wavelength method was less impacted by the change in ROSA size as evidenced by its RMSE, which remained up to four times lower than that of the two other methods.

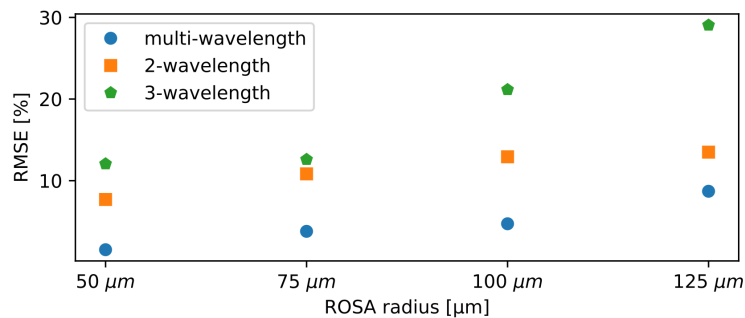


**Fig. 8.** Impact of ROSA size on  $\text{StO}_2$  calculations. RMSE of the relationships between the calculated and actual values as a function of ROSA radius. The two-, three-, and multi-wavelength methods were used for  $\text{StO}_2$  calculation.

## 4. Discussion

In this study, we demonstrated the robustness of multi-wavelength oximetry in the face of variations in acquisition parameters. This is one of the advantages of the two-step approach used for the determination of coefficients. While Eq. (1) can be resolved for a given spectrum using a least-squares method, with 6 unknowns to find the coefficients which fit that spectrum, this approach would not guarantee accuracy of the coefficients found. In fact, high coefficient accuracy is generally obtained when the number of terms in the equation is kept at minimum [36]. On the other hand, the two-step coefficient determination that we present makes a first estimate of the contribution of elements other than hemoglobin absorption to the optical density, allowing a second resolution for oxygenated and reduced hemoglobin with a low number of unknown

variables. The only condition remaining is to solve the equation in a range of wavelengths where the residuals of the first approximation have a lower impact. We found that the range between 530 nm and 585 nm was the most suitable and the one that leads to the most accurate  $\text{StO}_2$  values over the entire oxygen saturation range (Figs. 2 and 3). These results are in line with previous studies [26,27], which used regions between 510 nm and 590 nm, but assumed wavelength-independent scattering in the chosen spectral region. The improvement brought forward by our method is that it does not require assumptions on the  $\text{StO}_2$  value and the elements that affect optical density, but rather calculates it directly from the collected signal. This brings a substantial improvement to other previous multi-wavelength methods [42,54,55] that attempted to include all elements in the reflectance model and solve it all in one step - an approach that compromises the accuracy of oximetry calculation.

Sensitivity to various acquisition parameters is an important characteristic for any multifactor measurement method. In the case of  $\text{StO}_2$  calculations, we can see that the spectral resolution has a significant impact on accuracy (Figure 4); a low resolution leading to an underestimation of  $\text{StO}_2$ . This result could be explained by the fact that a low resolution leads to poorer localization of the peaks, valleys and inflection points essential to the distinction between oxygenated hemoglobin and reduced hemoglobin. Beach *et al.* observed that the use of a 60-nm bandwidth filter induced an 8% difference between the optical densities of oxygenated hemoglobin and reduced hemoglobin [48]. Still, the underestimation in  $\text{StO}_2$  observed in the present study remains low for resolutions below 6 nm. This robustness could be explained by the fact that multi-wavelength oximetry is not based on two or three specific wavelengths, but on a synergy of all the wavelength within the range considered.

We also showed that both shot noise (Figure 5 and Table 2) and Gaussian noises (Figure 6 and Table 3) have an effect on the accuracy of multi-wavelength oximetry. While the linearity of correlations between the calculated and the actual  $\text{StO}_2$  is not impacted, the distribution around the regression line is affected. This noise effect, although present, remains low compared to two- and three-wavelength methods (Figure 6). These results are in agreement with previous studies [36], including a number investigating error for the two-wavelength method [56,57]. Using a larger number of wavelengths increases the signal-to-noise ratio, which is inversely proportional to the square root of the number of wavelengths used [49].

Beyond the spectral range, spectral resolution and impact of the noise on the overall spectrum, it is interesting to determine the impact of noise affecting a single wavelength on oximetry measurements. This enables us to establish the relative contribution of each wavelength to the calculation of  $\text{StO}_2$  for the two-, three- and multi-wavelength methods. The trend of RMSE over the wavelengths disturbed for the multi-wavelength method highlights many insights. We found that 560 nm, which corresponds to a valley in the absorption spectrum of oxygenated hemoglobin, is given greater importance than 540 nm corresponding to the first peak in the region considered; that a disturbance at the isosbestic wavelength around 570 nm does not impact the accuracy whereas the ends of the spectral region are very sensitive. To our knowledge, there are no previous studies on the sensitivity to perturbations of multi-wavelength oximetry at each individual wavelength. Damodaran *et al.* used data collected on a retina-mimicking phantom to determine optimal wavelengths for oximetry, based on each wavelength's sensitivity to disturbance [57], but their study was applied only to the two-wavelength method, while Smith conducted a similar study applied to the three-wavelengths method [47]. Interestingly, our study demonstrates that both two- and three-wavelength oximetry approaches are very sensitive to noise applied to any of the wavelengths used for calculations, with disturbances of 1% in amplitude leading to RMSEs greater than that of disturbances of 20% applied to any wavelength in the multi-wavelength method. This highlights the robustness, and a major strength, of the latter method.

Finally, it was important to determine the impact of the ROSA overlapping with both a blood vessel and the surrounding tissue on the StO<sub>2</sub> measurements of blood in the vessels. The outcome is that the oximetry measurement is only slightly affected. The differences observed are due to the fact that when a portion of the ROSA is outside the blood vessel, a significant amount of light is backscattered towards the detector without having interacted with the hemoglobin, resulting in a modification of the collected reflectance spectrum [58,59]. Thus, the greater portion of the ROSA located outside the vessel, the more the collected spectrum is different from that of hemoglobin. These observations are in agreement with previous studies which observed that this effect called **pigment packing** had a fairly large impact on two-wavelength oximetry [57,60]. Despite the strong correlation between the proportion of the blood vessel in the ROSA (BV-ROSA ratio) and the error on StO<sub>2</sub>, the impact remains relatively weak and decreases rapidly with the increase in the proportion BV-ROSA ratio for multi-wavelength oximetry. This opens the door to reliable tissue oximetry, in which StO<sub>2</sub> measurements are made for small vessels located within tissue. The performance of our multi-wavelength method even when there is overlap with the background tissue could be explained by the absence of a priori assumptions in the method, which allows a good attenuation of adverse effects of background tissue scattering.

The approach and conclusions presented in this study are meant to be a first step in the selection of key components and parameters of the acquisition system. Specific simulations on the impact of optical system errors as well as post-design characterization experiments are additional steps that are obviously required in the development process of this type of system, but are outside the scope of this study.

## 5. Conclusion

We have shown the robustness of multi-wavelength oximetry to several spectral acquisition parameters. An appropriate choice of wavelength range and spectral resolution remain determinants, but other parameters can also affect the performance of the method. The results presented in this study identify these parameters and quantify their impacts. Moreover, the results can be used in the design of systems for the determination of StO<sub>2</sub> in the eye fundus and other tissues such as the skin and mucous membranes. The model strongly suggests the use of a wide spectral range which allows for accurate assessments of StO<sub>2</sub> in retinal microcapillaries, opening the door to the monitoring of local changes in hemodynamics through oximetry of ocular tissues.

**Funding.** National Research Council Canada - Industrial Research Assistance Program; Government of Canada Scientific Research and Experimental Development Tax Incentive Program.

**Disclosures.** Cl  ophas Akitegetse and Jasmine Poirier work for Zilia Inc, which funded this research. Dominic Sauvageau is CTO and co-founder of Zilia Inc.

**Data Availability.** Code and data underlying the results presented in this paper are not publicly available at this time, but may be obtained from the authors upon reasonable request.

**Supplemental document.** See [Supplement 1](#) for supporting content.

## References

1. P. Vaupel and L. Harrison, "Tumor hypoxia: causative factors, compensatory mechanisms, and cellular response," *The Oncologist* **9**(S5), 4–9 (2004).
2. P. Vaupel, A. B. Flood, and H. M. Swartz, "Oxygenation Status of Malignant Tumors vs. Normal Tissues: Critical Evaluation and Updated Data Source Based on Direct Measurements with pO<sub>2</sub> Microsensors," *Appl. Magn. Reson.* **52**(10), 1451–1479 (2021).
3. G. Xu, L. Dong, J. Yuan, Y. Zhao, M. Liu, M. Hui, and L. Kong, "Early Noninvasive Monitoring of Hypoxic State of Diabetic Foot Based on Diffuse Reflectance Spectroscopy," *Front. Phys.* **10**, 276 (2022).
4. E. C. S  nchez, "Pathophysiology of ischemia-reperfusion injury and its management with hyperbaric oxygen (HBO): a review," *J. Emerg. Crit. Care Med.* **3**, 22 (2019).
5. J. Boeckeaert, E. Vandewalle, and I. Stalmans, "Oximetry: recent insights into retinal vasopathies and glaucoma," *Bull. Soc. Belge Ophtalmol.* **319**, 75–83 (2012).
6. S. H. Hardarson, "Retinal Oximetry," *Acta Ophthalmologica* **91**, 1–47 (2013).

7. O. B. Olafsdottir, E. Vandewalle, L. A. Pinto, A. Geirsdottir, E. De Clerck, P. Stalmans, M. S. Gottfredsdottir, J. V. Kristjansdottir, J. Van Calster, T. Zeyen, E. Stefánsson, and I. Stalmans, "Retinal oxygen metabolism in healthy subjects and glaucoma patients," *Br. J. Ophthalmol.* **98**(3), 329–333 (2014).
8. L. A. Tobe, A. Harris, A. Schroeder, A. Gerber, S. Holland, A. Amireskandari, N. J. Kim, and B. Siesky, "Retinal Oxygen Saturation and Metabolism: How does it Pertain to Glaucoma? An Update on the Application of Retinal Oximetry in Glaucoma," *Eur. J. Ophthalmol.* **23**(4), 465–472 (2013).
9. E. Vandewalle, L. Abeg ao Pinto, O. B. Olafsdottir, E. De Clerck, P. Stalmans, J. Van Calster, T. Zeyen, E. Stefánsson, and I. Stalmans, "Oximetry in glaucoma: correlation of metabolic change with structural and functional damage," *Acta Ophthalmol.* **92**(2), 105–110 (2014).
10. D. J. Mordant, I. Al-Abboud, G. Muyo, A. Gorman, A. R. Harvey, and A. I. McNaught, "Oxygen saturation measurements of the retinal vasculature in treated asymmetrical primary open-angle glaucoma using hyperspectral imaging," *Eye* **28**(10), 1190–1200 (2014).
11. C. M. Jørgensen, S. H. Hardarson, and T. Bek, "The oxygen saturation in retinal vessels from diabetic patients depends on the severity and type of vision-threatening retinopathy," *Acta Ophthalmol.* **92**(1), 34–39 (2014).
12. S. H. Hardarson and E. Stefánsson, "Retinal oxygen saturation is altered in diabetic retinopathy," *Br. J. Ophthalmol.* **96**(4), 560–563 (2012).
13. A. Guduru, T. G. Martz, A. Waters, A. V. Kshirsagar, and S. Garg, "Oxygen saturation of retinal vessels in all stages of diabetic retinopathy and correlation to ultra-wide field fluorescein angiography," *Invest. Ophthalmol. Vis. Sci.* **57**(13), 5278–5284 (2016).
14. M. Hammer, W. Vilser, T. Riemer, A. Mandecka, D. Schweitzer, U. Kühn, J. Dawczynski, F. Liemt, and J. Strobel, "Diabetic patients with retinopathy show increased retinal venous oxygen saturation," *Graefe's Arch. Clin. Exp. Ophthalmol.* **247**(8), 1025–1030 (2009).
15. T. H. Williamson, J. Grewal, B. Gupta, B. Mokete, M. Lim, and C. H. Fry, "Measurement of PO<sub>2</sub> during vitrectomy for central retinal vein occlusion, a pilot study," *Graefe's Arch. Clin. Exp. Ophthalmol.* **247**(8), 1019–1023 (2009).
16. S. Yoneya, T. Saito, Y. Nishiyama, T. Deguchi, M. Takasu, T. Gil, and E. Horn, "Retinal oxygen saturation levels in patients with central retinal vein occlusion," *Ophthalmology* **109**(8), 1521–1526 (2002).
17. R. Battu, A. Mohan, A. Khanna, A. Kumar, and R. Shetty, "Retinal oxygen saturation in retinitis pigmentosa and macular dystrophies in Asian-Indian eyes," *Invest. Ophthalmol. Vis. Sci.* **56**(5), 2798 (2015).
18. R. I. Bojinova, D. F. Schorderet, C. Valmaggia, C. Türksever, A. Schoetza, and M. G. Todorova, "Higher retinal vessel oxygen saturation: investigating its relationship with macular oedema in retinitis pigmentosa patients," *Eye* **32**(7), 1209–1219 (2018).
19. A. Geirsdottir, S. H. Hardarson, O. B. Olafsdottir, and E. Stefánsson, "Retinal oxygen metabolism in exudative age-related macular degeneration," *Acta Ophthalmol.* **92**(1), 27–33 (2014).
20. G. G. Stokes, "On the reduction and oxidation of the colouring matter of the blood," *Proc. R. Soc. Lond.* **13**, 355–364 (1864).
21. T. Aoyagi, "Pulse oximetry: its invention, theory, and future," *J. Anesthesia* **17**(4), 259–266 (2003).
22. J. Beach, "Pathway to retinal oximetry," *Trans. Vis. Sci. Technol.* **3**(5), 2 (2014).
23. G. A. Millikan, "The oximeter, an instrument for measuring continuously the oxygen saturation of arterial blood in man," *Rev. Sci. Instrum.* **13**(10), 434–444 (1942).
24. P. Sekelj, D. Eng, A. L. Johnson, H. E. Hoff, and M. P. Schuerch, "A photoelectric method for the determination of arterial oxygen saturation in man," *Am. Heart J.* **42**(6), 826–848 (1951).
25. J. B. Hickam, R. Frayser, and J. C. Ross, "A study of retinal venous blood oxygen saturation in human subjects by photographic means," *Circulation* **27**(3), 375–385 (1963).
26. R. N. Pittman and B. R. Duling, "A new method for the measurement of percent oxyhemoglobin," *J. Appl. Phys.* **38**(2), 315–320 (1975).
27. F. C. Delori, "Noninvasive technique for oximetry of blood in retinal vessels," *Appl. Opt.* **27**(6), 1113 (1988).
28. A. A. Strattonnikov and V. B. Loschenov, "Evaluation of blood oxygen saturation in vivo from diffuse reflectance spectra," *J. Biomed. Opt.* **6**(4), 457 (2001).
29. D. Schweitzer, L. Leistritz, M. Hammer, M. Scibor, U. Bartsch, and J. Strobel, "Calibration-free measurement of the oxygen saturation in human retinal vessels," *Proc. SPIE* **2393**, 210 (1995).
30. A. Sircan-Kucuksayan, M. Uyuklu, and M. Canpolat, "Diffuse reflectance spectroscopy for the measurement of tissue oxygen saturation," *Physiol. Meas.* **36**(12), 2461–2469 (2015).
31. S. Chen, J. Yi, and H. F. Zhang, "Measuring oxygen saturation in retinal and choroidal circulations in rats using visible light optical coherence tomography angiography," *Biomed. Opt. Express* **6**(8), 2840 (2015).
32. F. Hu, K. Vishwanath, J. Lo, A. Erkanli, C. Mulvey, W. T. Lee, and N. Ramanujam, "Rapid determination of oxygen saturation and vascularity for cancer detection," *PLoS One* **8**(12), e82977 (2013).
33. D. Yudovsky and L. Pilon, "Rapid and accurate estimation of blood saturation, melanin content, and epidermis thickness from spectral diffuse reflectance," *Appl. Opt.* **49**(10), 1707–1719 (2010).
34. S. Takatani and M. D. Graham, "Theoretical analysis of diffuse reflectance from a two-layer tissue model," *IEEE Trans. Biomed. Eng.* **BME-26**(12), 656–664 (1979).
35. M. Hammer, E. Thamm, and D. Schweitzer, "A simple algorithm for in vivo ocular fundus oximetry compensating for non-haemoglobin absorption and scattering," *Phys. Med. Biol.* **47**(17), N233–N238 (2002).



36. D. T. DePaoli, P. Tossou, M. Parent, D. Sauvageau, and D. C. Côté, "Convolutional neural networks for spectroscopic analysis in retinal oximetry," *Sci. Rep.* **9**(1), 11387 (2019).
37. C. Akitegetse, P. Landry, J. Robidoux, N. Lapointe, D. Brouard, D. Sauvageau, and D. Sauvageau, "Monte-Carlo simulation and tissue-phantom model for validation of ocular oximetry," *Biomed. Opt. Express* **13**(5), 2929–2946 (2022).
38. S. Jacques, T. Li, and S. Prahl, "mcxyz. c, a 3D Monte Carlo simulation of heterogeneous tissues," (2019).
39. M. Hammer and D. Schweitzer, "Quantitative reflection spectroscopy at the human ocular fundus," *Phys. Med. Biol.* **47**(2), 179–191 (2002).
40. S. J. Preece and E. Claridge, "Monte Carlo modelling of the spectral reflectance of the human eye," *Phys. Med. Biol.* **47**(16), 3032863 (2002).
41. M. Hammer, A. Roggan, D. Schweitzer, and G. Muller, "Optical properties of ocular fundus tissues-an in vitro study using the double-integrating-sphere technique and inverse Monte Carlo simulation," *Phys. Med. Biol.* **40**(6), 963–978 (1995).
42. M. Desjardins, J. P. Sylvestre, R. Jafari, S. Kulasekara, K. Rose, R. Trussart, J. D. Arbour, C. Hudson, and F. Lesage, "Preliminary investigation of multispectral retinal tissue oximetry mapping using a hyperspectral retinal camera," *Exp. Eye Res.* **146**, 330–340 (2016).
43. V. Vucea, P. J. Bernard, P. Sauvageau, and V. Diaconu, "Blood oxygenation measurements by multichannel reflectometry on the venous and arterial structures of the retina," *Appl. Opt.* **50**(26), 5185–5191 (2011).
44. S. L. Jacques and B. W. Pogue, "Tutorial on diffuse light transport," *J. Biomed. Opt.* **13**(4), 041302 (2008).
45. J. J. Davenport, J. Hodgkinson, J. R. Saffell, and R. P. Tatam, "Noise analysis for CCD-based ultraviolet and visible spectrophotometry," *Appl. Opt.* **54**(27), 8135 (2015).
46. B. Jones, "Low-frequency noise spectroscopy," *IEEE Trans. Electron Devices* **41**(11), 2188–2197 (1994).
47. M. H. Smith, "Optimum wavelength combinations for retinal vessel oximetry," *Appl. Opt.* **38**(1), 258 (1999).
48. J. M. Beach, K. J. Schwenzer, S. Srinivas, D. Kim, and J. S. Tiedeman, "Oximetry of retinal vessels by dual-wavelength imaging: calibration and influence of pigmentation," *J. Appl. Phys.* **86**(2), 748–758 (1999).
49. D. Schweitzer, E. Thamm, M. Hammer, and J. Kraft, "A new method for the measurement of oxygen saturation at the human ocular fundus," *Int. Ophthalmol.* **23**(4/6), 347–353 (2001).
50. B. Khoobehi, J. M. Beach, and H. Kawano, "Hyperspectral imaging for measurement of oxygen saturation in the optic nerve head," *Invest. Ophthalmol. Visual Sci.* **45**(5), 1464–1472 (2004).
51. J. C. Ramella-Roman and S. A. Mathews, "Spectroscopic measurements of oxygen saturation in the retina," *IEEE J. Sel. Top. Quantum Electron.* **13**(6), 1697–1703 (2007).
52. Y. Guo, G. Yao, B. Lei, and J. Tan, "Monte Carlo model for studying the effects of melanin concentrations on retina light absorption," *J. Opt. Soc. Am. A* **25**(2), 304 (2008).
53. N. Lapointe, C. Akitegetse, J. Poirier, M. Picard, P. Sauvageau, and D. Sauvageau, "Targeted spectroscopy in the eye fundus," *bioRxiv*, 2023.04.27.538643 (2023).
54. D. Schweitzer, M. Hammer, J. Kraft, E. Thamm, E. Konigsdorffer, and J. Strobel, "In vivo measurement of the oxygen saturation of retinal vessels in healthy volunteers," *IEEE Trans. Biomed. Eng.* **46**(12), 1454–1465 (1999).
55. V. Diaconu, "Multichannel spectrophotometry: A noninvasive method for assessment of on-line hemoglobin derivatives," *Appl. Opt.* **48**(10), D52–D61 (2009).
56. M. Marois, S. L. Jacques, and K. D. Paulsen, "Optimal wavelength selection for optical spectroscopy of hemoglobin and water within a simulated light-scattering tissue," *J. Biomed. Opt.* **23**(04), 041202 (2018).
57. M. Damodaran, A. Amelink, and J. F. de Boer, "Optimal wavelengths for subdiffuse scanning laser oximetry of the human retina," *J. Biomed. Opt.* **23**(08), 086003 (2018).
58. J. C. Finlay and T. H. Foster, "Effect of pigment packaging on diffuse reflectance spectroscopy of samples containing red blood cells," *Opt. Lett.* **29**(9), 965 (2004).
59. N. Rajaram, A. Gopal, X. Zhang, and J. W. Tunnell, "Experimental validation of the effects of microvasculature pigment packaging on in vivo diffuse reflectance spectroscopy," *Lasers Surg. Med.* **42**(7), 680–688 (2010).
60. M. Damodaran, A. Amelink, F. Feroldi, B. Lochocki, V. Davidoiu, and J. F. d. Boer, "In vivo subdiffuse scanning laser oximetry of the human retina," *J. Biomed. Opt.* **24**(09), 1 (2019).